Physicochem. Probl. Miner. Process., 62(4), 2026, 226664

http://www.journalssystem.com/ppmp

Physicochemical Problems of Mineral Processing

ISSN 1643-1049

Flotation froth image segmentation based on an improved watershed algorithm with highlight overlap correction and multiple edge constraints

Lirong Yang [1,2], Zhiwen Huang [1], Xiaolong Zhu [1], Cong Sun [1]

[1] College of Mechanical and Electrical Engineering，Jiangxi University of Science and Technology, Ganzhou 341000, Jiangxi China

[2] Jiangxi Provincial Key Laboratory of Particle Technology, Nanchang 330013, Jiangxi China

Corresponding author: 1652523957@qq.com (Lirong Yang)

Abstract: Accurate segmentation of froth images is crucial for online monitoring of flotation performance. However, uneven illumination, specular highlight overlap and low-contrast edges frequently cause over-segmentation and under-segmentation when classical watershed transform is applied. In this study, an improved watershed algorithm incorporates specular highlight overlap correction and multi-directional edge constraints. First, Intuitionistic Fuzzy C-means (IFCM), adaptive thresholding and open-close morphological reconstruction are combined to extract and classify highlights into small, medium and large bubbles. An overlap-correction fusion strategy is then designed to remove spurious markers. Second, horizontal–vertical edges extracted by Laplacian of Gaussian (LoG) and ±45° edges obtained by diagonal gradient filters are merged to generate a complete constraint line. Finally, the fused markers and the edge-preserving constraint line are fed into a marker-controlled watershed, achieving robust segmentation of multi-scale froth images. Experiments on 50 on-site images from a tungsten–molybdenum flotation plant show that the proposed method yields mean Adjusted Rand Index (ARI) values of 81.85 %, 87.63 % and 91.63 % for small, medium and large bubbles, respectively, outperforming two state-of-the-art watershed variants.

Keywords: froth image, highlight overlap correction, edge constraints, watershed segmentation algorithm

1. Introduction

Froth morphology, especially bubble size distribution, is a key indicator of flotation performance (Morar et al., 2012). Real-time segmentation of froth images enables automatic control of reagent dosage and air flow rate, thereby improving concentrate grade and recovery (Aldrich et al., 2011). Nevertheless, on-site froth images suffer from three major challenges: (i) uneven illumination generated by multiple overhead lamps produces several specular highlights that are not centrally located inside bubbles; (ii) low contrast between adjacent bubbles produces blurred or missing edges; and (iii) stacked bubbles of different sizes aggravate over-segmentation when conventional watershed transform is used (Bhondayi et al., 2022, Guo et al., 2022).

To alleviate these problems, researchers have introduced marker-controlled watershed algorithms in which reliable foreground markers and external constraint lines are prerequisites. Liang et al. (2020) applied fuzzy C-means (FCM) clustering to highlight regions and subsequently corrected markers according to bubble size, yet noise-induced false markers were not thoroughly removed.

In the present work, an improved-watershed approach is proposed. The main contributions are three-fold:

(1) A triple-source marker-extraction scheme (IFCM, adaptive thresholding, open-close reconstruction) followed by size-dependent overlap correction is designed to provide high-purity foreground markers.

(2) Multi-directional edge constraints (0°, 90°, +45°, −45°) are integrated to reconstruct closed and

DOI: 10.37190/ppmp/226664

continuous constraint lines, significantly reducing edge leakage.

(3) Exhaustive experiments on 50 representative froth images demonstrate that the proposed method outperforms two latest watershed variants in terms of ARI.

The remainder of this paper is organized as follows: Section 1 reviews the related work. Section 2 introduces the fundamental principles of the algorithms employed in this study. Section 3 elaborates on the proposed improvements to the watershed framework, specifically the implementation of highlight-overlap correction and multi-directional edge constraints. Section 4 presents the experimental dataset, results and analysis. Finally, Section 5 provides a conclusion to the study.

1.1. Related work

The main challenge for the watershed transform remains over-segmentation caused by image noise. To tame this defect, four research lines have evolved: (i) optimal-marker, (ii) edge-constrained, (iii) region-merging, and (iv) deep-learning-coupled watersheds.

Zhang et al. (2011) generated markers via distance transform followed by morphological reconstruction, drastically reducing redundant basins. Jahedsaravani et al. (2014) proposed a marker-controlled watershed algorithm to reduce over-segmentation of froth images. Lang et al. (2011) combined Phansalkar binarization with block-contour-derived seeds to disentangle bubbles that are adhesive, overlapping, or blurred. Moga et al. (1998) calibrated an elasticity-based oversegmentation through external markers. Nevertheless, when bubble boundaries are faint, marker-only watersheds are markedly inferior to "marker-plus-constraint" counterparts, making the latter the mainstream paradigm in froth segmentation.

Nassir Salman et al. (2006) integrated K-means, watershed, and Difference-of-Intensities (DIS) maps to perform simultaneous segmentation and edge detection. Ding et al. (2024) Gaussian-filtered the image, produced an intentionally oversegmented edge map, and used it as the substrate for subsequent merging.

Zhang et al.**Błąd! Nie można odnaleźć źródła odwołania.** (2008) extracted regional minima via H-dome reconstruction and used them as watershed seeds. Rapaka et al. (2021) refined this pipeline by inserting a modified FCM clustering step, yielding impressive accuracy for tiny bubbles. Yet, when froths exhibit low contrast and bright rims, FCM fails to suppress non-bubble bright spots. Xie et al. (2019) further introduced a fast thresholding segmentation method derived from pixel distribution characteristics to initialize marker generation, though its performance remained limited under non-uniform illumination. Liang et al. (2020) clustered and merged similar highlights to create foreground markers, but noise and bright edges still shift the dividing lines. Among the follow-ups, Zhang et al. (2019) refined marker generation for the watershed, while Peng et al. (2021) first extracted bubble boundaries with edge operators and then treated them as external constraints; fusing these constraints with foreground markers produced optimal dividing surfaces. Zhang et al. (2022) proposed region-adaptive, multi-scale Retinex compensation to equalize brightness and suppress noise as well as bright-edge artifacts.

On the deep-learning side, Tang et al. (2023) proposed I-Attention U-Net—an Inception-augmented U-Net that suppresses both under- and oversegmentation after training on flotation images. Xue et al. (2023) achieved accurate image segmentation by combining an improved watershed algorithm with a U-Net neural network model. Chen et al. (2024) boosted instance segmentation through image-enhancement and color-shift cancellation modules. Although each method is effective in isolation, limited synergy prevents reliable performance on low-contrast, complex froths.

Yet even these state-of-the-art remedies still break down on froths with barely visible edges and extremely low contrast. we explicitly model ±45° diagonal edges and merge them with Laplacian-of-Gaussian (LoG) responses to form a closed constraint line. Furthermore, a size-adaptive overlap-correction module is proposed to eliminate false markers-an aspect absent in previous studies.

2. Fundamental principles

2.1 Principle of MSRCR

The Multi-Scale Retinex with Color Restoration (MSRCR) algorithm is an advanced extension and application of Retinex theory. According to Retinex theory, an image $I(x, y)$ can be decomposed into a reflectance image $R(x, y)$ and an illumination image $L(x, y)$, as follows:

$$I(x,y) = R(x,y) \times L(x,y) \tag{1}$$

where $I(x,y)$ represents the image signal captured by the observer or camera;$R(x,y)$denotes the reflectance component that carries the detailed information of the target object; and $L(x,y)$ represents the illumination component of ambient light, which should be suppressed or removed as much as possible.

To extract the reflectance information, a logarithmic transformation is applied to both sides of the equation:

$$Log[R(x,y)] = L\log[I(x,y)] - Log[L(x,y)] \tag{2}$$

Building upon this, MSRCR introduces a color restoration factor C to recover the chromatic information of the image. The MSRCR formula is expressed as:

$$MSRCR(x,y) = C(x,y) \times R_{MSR}(x,y) \tag{3}$$

where $C(x,y)$ is the color restoration factor derived from the statistical processing of the image's color channels:

$$C(x,y) = \beta \log\left[\alpha \frac{I(x,y)}{\sum I(x,y)}\right] \tag{4}$$

where, β is a gain constant used to adjust the intensity of color restoration, and α is a parameter controlling non-linearity to ensure that the input to the logarithmic function remains positive. β and α are assigned values of 46 and 125, respectively.

$R_{MSR}(x,y)$ is the result of multi-scale Retinex processing, calculated as:

$$R_{MSR}(x,y) = \sum_{k=1}^{N} w_k \, R_{SSR_k}(x,y) \tag{5}$$

where $R_{SSR_k}(x,y)$ is the Single-Scale Retinex (SSR) result computed using the k-th Gaussian scale, and w_k is the weight assigned to that scale. The calculation for $R_{SSR_k}(x,y)$ is:

$$R_{SSR_k}(x,y) = \frac{I(x,y)}{I(x,y) * G_{\sigma_k}(x,y)} \tag{6}$$

In this formula,$G_{\sigma_k}(x,y)$is the Gaussian kernel, which serves as a discrete digital representation of a two-dimensional Gaussian function in space. $\sigma$is the standard deviation of the Gaussian distribution, defining the operational scale of the Gaussian kernel. In this work, the standard deviation σ is set to 1.2.The principle of the Gaussian kernel is as follows:

$$G_{\sigma_k}(x,y) = \frac{1}{2\pi\sigma^2} e^{-\frac{x^2+y^2}{2\sigma^2}} \tag{7}$$

2.2. Principle of IFCM

The IFCM algorithm is an extension of the traditional Fuzzy C-Means (FCM) algorithm. By introducing three indices—membership, non-membership, and hesitation degrees—it precisely describes the uncertainty of a pixel belonging to a specific category.

2.2.1. Feature space construction and similarity measurement

The pixels of the image to be processed are transformed into a set of data points in a feature space,$X = \{x_1, x_2, \ldots, x_N\}$, where x_i is defined as the feature vector of the i-th pixel and c_j is the feature value of the j-th cluster center. The similarity between data point x_i and cluster center c_j is measured by their Euclidean distance d_{ij} in the feature space:

$$d_{ij} = \| x_i - c_j \| \tag{8}$$

A smaller distance indicates that the pixel is more similar to the features represented by that cluster.

2.2.2. Definition of intuitionistic fuzzy parameters

For each pixel x_i and each cluster j, the IFCM algorithm defines three parameters to describe their relationship, satisfying the following constraint:

$$u_{ij} + v_{ij} + \pi_{ij} = 1 \tag{9}$$

where the membership degree u_{ij} represents the extent to which pixel i belongs to cluster j; the non-membership degree v_{ij} represents the extent to which it does not; and the hesitation degree π_{ij}

represents the uncertainty regarding its membership. This is a key advantage of IFCM over FCM, as it better handles fuzzy boundaries.

2.2.3. Construction of the objective function

The core of the IFCM algorithm is to minimize an objective function J_{IFCM} through iterative optimization to achieve optimal clustering:

$$J_{IFCM} = \sum_{i=1}^{N} \sum_{j=1}^{C} \left(u_{ij}^{*}\right)^{m} \parallel x_i - c_j \parallel^2 + \sum_{i=1}^{N} \pi_i^{o} \tag{10}$$

where N is the total number of data points; C is the predefined number of clusters; u_{ij}^{*} is the modified membership degree (defined as $u_{ij}^{*} = u_{ij} + \pi_{ij}$), which reflects the concept of converting the hesitation part into membership; m is the fuzziness weighting exponent that controls the degree of clustering fuzziness; and π_i^{o} is the hesitation-induced regularization term used to limit the distribution of uncertainty during clustering. Parameters N and C are both assigned a value of 2.

2.2.4. Iterative update of cluster centers and membership

The algorithm seeks the optimal solution through an iterative process that alternately updates the membership parameters and cluster centers until the objective function converges. The new cluster center is the weighted average of all pixel feature vectors within that category:

$$c_j = \frac{\sum_{i=1}^{N} \left(u_{ij}^{*}\right)^{m} x_i}{\sum_{i=1}^{N} \left(u_{ij}^{*}\right)^{m}} \tag{11}$$

The membership update formula is as follows:

$$u_{ij} = \frac{1}{\sum_{k=1}^{C} \left(\frac{\parallel x_i - c_j \parallel}{\parallel x_i - c_k \parallel}\right)^{\frac{2}{m-1}}} \tag{12}$$

where c_k is the index in the denominator summation representing all cluster centers (from 1 to C).

2.2.5. Generation of initial highlight markers

Iteration stops when the convergence condition is met (i.e., the change in the objective function is minimal). At this point, pixels undergo hard partitioning based on the maximum membership principle to identify highlight regions:

$$Markers = \{x_i \mid \mathrm{class}(x_i) = C_{highlight}\} \tag{13}$$

where $C_{highlight}$ is the cluster representing highlights. By analyzing the feature values of the final cluster centers c_j, the cluster representing the highlight region is identified. The set of all pixels x_i assigned to this cluster constitutes the final initial highlight markers (Markers).

2.3 Adaptive thresholding method (ATM)

Instead of using a uniform global threshold, this algorithm dynamically calculates a threshold for each pixel based on the grayscale distribution within its local neighborhood. This approach effectively distinguishes highlights from the background in localized regions, allowing for the precise extraction of initial markers. The principles are as follows:

2.3.1. Neighborhood definition

A neighborhood window $W(x, y)$ of size $N \times N$ is defined, centered on the target pixel $I(x, y)$ in the image. This neighborhood serves as the basis for calculating the local threshold, and its window size is a critical parameter influencing the algorithm's performance. In this work,W is set to 25×25.

2.3.2. Local threshold calculation

Within the neighborhood window $W(x, y)$, a dynamic threshold $T(x, y)$， is statistically computed. The method involves calculating the mean (or Gaussian-weighted mean) of all pixel grayscale values within the neighborhood and subtracting a constant C for fine-tuning:

$$T(x,y) = mean\big(W(x,y)\big) - C \tag{14}$$

where $mean\big(W(x,y)\big)$ is the average grayscale value within the window $W(x,y)$, and C is an empirical constant used to compensate for the deviation between the mean and the ideal threshold，C is set to 5.

2.3.3. Pixel binarization

The grayscale value of the central pixel $I(x,y)$ is compared with the calculated local threshold $T(x,y)$ to determine whether it is a highlight point. The decision logic is as follows:

$$O(x,y) = \begin{cases} L_{max} & \text{If} I(x,y) > T(x,y) \\ 0 & \text{otherwise} \end{cases} \tag{15}$$

where $O(x,y)$ represents the pixel value in the resulting binary image.

2.3.4. Image traversal and threshold application

By sliding the neighborhood window W, steps 1 through 3 are repeated for every pixel in the input image I. This ensures that a unique local threshold is calculated and applied to each individual pixel.

2.3.5. Generation of initial highlight markers

After traversing the entire image, a binary image O is obtained. In this image, all pixels with a value of 255 constitute the extracted highlight regions. The set of these regions forms the initial highlight markers (Markers).

$$Markers = (x,y)|O(x,y) = 255 \tag{16}$$

2.4. Morphological reconstruction based on opening-and-closing operators (MROC)

Morphological reconstruction generates a marker image through erosion and subsequently reconstructs highlight morphologies via dilation under the constraint of the original mask image. The principles are as follows:

2.4.1. Generation of mask and marker images

The original froth grayscale image I is defined as the mask image (Mask).A structuring element B is selected to perform morphological erosion on imageIyielding the marker image J :

$$J = Erosion(I,B) \tag{17}$$

This step removes all highlight spots smaller than the structuring element B（a circular operator with a radius of 3）and causes larger highlight regions to shrink.

2.4.2. Dilation-based reconstruction

Using marker image J as the starting point and mask image I as the constraint, iterative geodesic dilation is performed until the image no longer changes. In each iteration, the result is capped by the grayscale values of the corresponding pixels in the mask image. The iteration formula is:

$$R_k + 1 = Dilation(R_k, B) \cap I \tag{18}$$

where $R_k = J$; "Dilation" denotes standard morphological dilation, and ∩ represents the pixel-wise minimum operation. The final image obtained upon convergence is the reconstructed image R，at this stage, small bright noise is completely eliminated, while authentic highlight regions are fully preserved, maintaining edges and grayscale values identical to the original image.

2.4.3. Separation of highlights and background

The reconstructed image R effectively eliminates high-frequency bright noise and serves as the background-suppressed, highlight-enhanced image $I_f$iltered.This process ensures that grayscale plains in the background are significantly suppressed, allowing prominent highlight targets to be clearly extracted:

$$I_f iltered = R \tag{19}$$

The logic of background suppression is that non-target areas failing to meet the size requirements of structuring element B (such as minor background fluctuations or grayscale spikes) are removed, making highlight features more prominent in the grayscale space.

2.4.4. Generation of initial highlight markers

A global threshold T_global （200）is applied to the background-suppressed reconstructed image R，to binarize the highlight regions, generating the final initial markers (Markers):

$$Markers = (x, y)|R(x, y) > T_global \tag{20}$$

2.5. Laplacian of Gaussian (LoG) operator

The LoG operator functions by first applying a Gaussian filter to smooth the image, thereby mitigating the influence of noise on the subsequent Laplacian operation. By integrating the properties of both Gaussian filtering and the Laplacian operator, this method effectively preserves fine edge details while reducing pseudo-edge responses triggered by noise during edge extraction.The isotropic Gaussian distribution for an image is defined as:

$$G(x, y, \sigma) = \frac{1}{2\pi\sigma^2} e^{-\frac{x^2+y^2}{2\sigma^2}} \tag{21}$$

The Laplacian transformation of an image is expressed as:

$$L(x, y) = \frac{\partial^2 I}{\partial x^2} + \frac{\partial^2 I}{\partial y^2} \tag{22}$$

where L(x, y) represents the image intensity information. By summing the second-order partial derivatives of the Gaussian filter in the X and Y directions, the Laplacian of Gaussian (LoG) operator is established.

$$LoG = \Delta G_\sigma(x, y, \sigma) = \frac{x^2+y^2-2\sigma^2}{\sigma^4} e^{-(x^2+y^2)/2\sigma^2} \tag{23}$$

3. An improved watershed algorithm for flotation forth image segmentation

To achieve accurate segmentation of froth images under conditions of uneven illumination and tight adhesion, this paper proposes an improved watershed segmentation algorithm that integrates multi-algorithm-optimized foreground markers and multi-operator edge constraints. Utilizing the classical watershed algorithm as the core framework, the proposed method enhances the segmentation performance for complex froth images by optimizing two critical inputs: foreground markers and edge constraints.To obtain high-confidence foreground markers, a multi-algorithm fusion scheme is designed. This approach classifies marker regions according to froth size and leverages the complementary strengths of Intuitionistic Fuzzy C-Means (IFCM), adaptive thresholding, and morphological reconstruction. To enhance the edge constraint effect, the algorithm fuses the Laplacian of Gaussian (LoG) operator with 45°gradient operators to construct a complete froth contour. Furthermore, it innovatively utilizes the extracted foreground markers to eliminate specular pseudo-edges, ensuring accurate boundary extraction in complex scenarios.

The overall framework of the proposed floatation froth image segmentation method is illustrated in Fig.1.

3.1. Froth image enhancement based on MSRCR algorithm

To address the issues of uneven brightness, low contrast, and blurred boundaries caused by non-uniform lighting and water vapor in flotation environments, this paper employs the Multi-Scale Retinex with Color Restoration (MSRCR) algorithm and Non-Local Means (NLM) filtering for preprocessing. The specific steps are as follows:

(1) MSRCR Adaptive Enhancement: Using the original froth image as input, multi-scale Gaussian kernels are applied to remove uneven incident light components and enhance intrinsic reflection properties. A color restoration factor is calculated to correct chromatic distortion induced by multi-scale processing, yielding an enhanced image with uniform illumination and natural color.

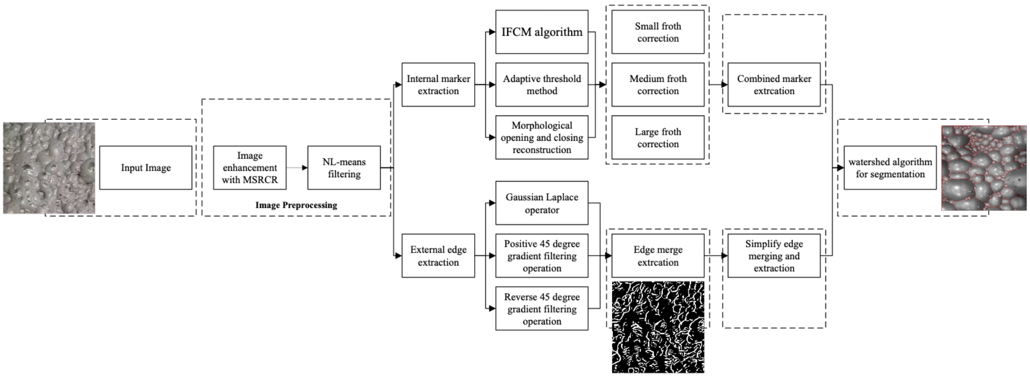

Fig. 1. Overall framework of the improved watershed segmentation method for floatation froth image

(2) NLM Smoothing and Denoising: The enhanced image is processed using the NLM algorithm by setting the search window size（21×21）and filtering strength（20）. Within the search window, patch similarities between the central pixel and its neighbors are calculated as weights for averaging. This effectively smoothes complex textures within specular highlights and small froth regions while preserving sharp boundaries between froths.
(3) Output: The final optimized image, processed by both MSRCR and NLM, features balanced brightness, high contrast, and smooth textures. This provides a robust foundation for high-precision foreground marker extraction and edge-constrained segmentation.

3.2. Overlap correction and specular highlight marker extraction via multi-algorithm fusion

Due to chaotic lighting environments in flotation sites, captured froth images often contain irregular specular highlights. Using a single algorithm for highlight extraction frequently leads to incomplete detection or over-segmentation. To address this, this paper proposes a foreground marker extraction method based on the complementary fusion of multiple algorithms. By implementing overlap correction and area merging on markers from three different algorithms, the optimal foreground markers for the improved segmentation algorithm are obtained. This method enhances marker accuracy when dealing with complex adherent froths. The specific process is described as follows:
(1) Parallel Generation of Initial Markers: IFCM, adaptive thresholding, and morphological reconstruction via opening-and-closing operators are applied in parallel to the preprocessed froth image to generate three sets of initial highlight marker maps.
(2) Classification of Marker Regions: The marker regions in each map are classified into small, medium, and large froth regions based on their connected component areas.
(3) Fusion and Overlap Correction: To integrate the advantages of the three extraction algorithms, overlap correction and area merging are performed on the marker regions of different sizes to extract the final foreground markers. The specific steps are as follows:

3.2.1. Small froth marker combination

To capture potential highlights, the small froth regions extracted by the Adaptive Thresholding (ATM) and Morphological Reconstruction (MROC) are first merged. This combined region is then intersected with the high-confidence marker regions from the IFCM algorithm to obtain the combined small froth markers $\mathrm{M_s}$. The calculation is as follows:

$$M_s = M_{s1} \cap (M_{s2} \cup M_{s3}) \tag{24}$$

where $\mathrm{M_{s1}}$, $\mathrm{M_{s2}}$, $\mathrm{M_{s3}}$ represent the small froth marker regions extracted by IFCM, ATM, and MROC, respectively.

3.2.2. Medium froth marker combination

Regions in the IFCM marker map with an area exceeding a specific threshold are extracted and intersected with the union of the ATM and MROC marker regions to obtain the combined medium froth markers $\mathrm{M_m}$:

$$M_m = (M_{m2} \cup M_{m3}) \cap M_{m1}(QS(M_{m1}) > S_{thre}) \tag{25}$$

where M_{m1},M_{m2}, and M_{m3} are the medium froth marker regions from IFCM, ATM, and MROC, respectively. The function QS calculates the area of connected components within the marker map. The area threshold S_{thre} is determined by analyzing the froth size distribution via IFCM clustering results; it is typically set to 50%–70% of the average medium froth area to filter out excessively small noise while retaining valid medium froth markers.

3.2.3. Large froth marker combination

Large froth regions are characterized by low noise but exhibit variations in boundaries across different algorithms. Therefore, the large froth regions from all three algorithms are merged (union) to form the combined large froth markers M_b:

$$M_b = M_{b1} \cup M_{b2} \cup M_{b3} \tag{26}$$

where M_{b1},M_{b2}, and M_{b3} represent the large froth marker regions from IFCM, ATM, and MROC, respectively.

3.2.4. Overall marker combination

After independently combining the markers for small, medium, and large froth regions, a final merging process is performed to obtain the optimal marker M, which serves as the required foreground marker for the segmentation algorithm:

$$M = M_s \cup M_m \cup M_b \tag{27}$$

where M_s,M_m, and M_b are the optimized marker combinations for small, medium, and large froth, respectively.

3.3. Edge constraint improvement

Traditional edge detection methods, such as individual Sobel or Canny operators, struggle to extract complete froth boundaries. To address this issue, this paper proposes a froth edge extraction method based on multi-operator fusion. Building upon the Laplacian of Gaussian (LoG) operator, ±45°gradient filtering operators are introduced to extract multi-directional gradients. By applying morphological constraints using the previously extracted foreground markers, invalid edges caused by specular highlights are eliminated, allowing the method to comprehensively capture edge information across horizontal, vertical, and diagonal directions. The specific procedure is as follows:

3.3.1. Parallel feature extraction

The LoG operator and ±45°gradient filtering operators are applied in parallel to the froth image to extract edge features from different directions.The extraction process is as follows：

$$E_{LoG} = \nabla^2[G(x,y,\sigma) * I(x,y)] \tag{28}$$

$$E_{+45} = I(x,y) * K_{+45} \tag{29}$$

$$E_{-45} = I(x,y) * K_{-45} \tag{30}$$

where $I(x,y)$ represents the preprocessed froth image, K_{+45} and K_{-45} represent the positive and negative 45°convolution kernels, $*$ denotes the convolution operation, ∇^2 is the Laplacian operator, and $G(x,y,\sigma)$ is the Gaussian smoothing function.

3.3.2. Initial map generation

The extraction results from the three operators are merged and processed through morphological erosion and dilation to form an initial complete edge map $E_{initial}$ .The process is as follows：

$$E_{merged} = E_{LoG} \cup E_{+45} \cup E_{-45} \tag{31}$$

$$E_{initial} = \left(E_{merged} \ominus B_1\right) \oplus B_1 \tag{32}$$

where ∪ denotes the pixel-wise union (or maximum value) operation, ⊖ and ⊕ represent morphological erosion and dilation, respectively, and B_1 （a 3×3 square operator） is the defined structuring element.

3.3.3. Marker dilation

To ensure comprehensive coverage of pseudo-edges generated by highlight regions, the extracted foreground marker M undergoes a dilation process of a specific size to obtain the coverage mask M_{mask}.

$$M_{mask} = M \oplus B_2 \tag{33}$$

where B_2 is the dilation structuring element. Its size must satisfy the constraint (highlight < B_2 < Forth_Edge) to ensure that pseudo-edges from highlights are fully covered without encroaching upon the actual foam boundaries. In this sthdy， B_2 is set to 6 pixels.

3.3.4. Interference elimination

The dilated marker mask is used to remove invalid internal edges from the initial edge map, resulting in the refined edge constraints $E_{refined}$ for the watershed algorithm:

$$E_{refined} = E_{initial} \cap \text{not}(M_{mask}) \tag{34}$$

4. Experiment and analysis

The experimental data used in this study were obtained from field videos captured at a tungsten-molybdenum flotation plant in Jiangxi. The recording duration was set to 20 seconds with a 30-minute sampling interval. From the database, seven video segments were randomly selected, and two images were extracted from each segment at a resolution of 260×260 pixels. As a well-equipped facility representative of standard flotation operations in China, the experimental results derived from this dataset possess substantial practical relevance for the domestic flotation industry.

4.1 Froth image enhancement and filtering

The MSRCR algorithm is employed to enhance the flotation froth images, followed by the Non-Local Means (NLM) filtering algorithm for smoothing. This process integrates froth textures with specular highlights, thereby facilitating the subsequent extraction of foreground markers. The results of the froth image enhancement and filtering are illustrated in Fig. 2.

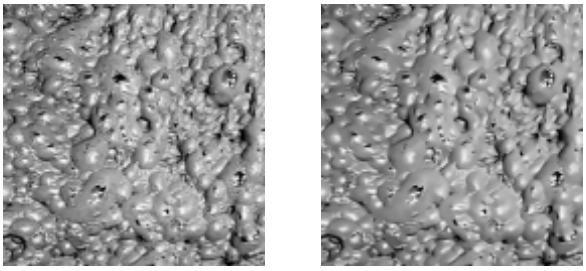

MSRCR enhancement effect NLM filtering effect

Fig. 2. Results of froth image enhancement and filtering

4.2. Highlight-overlap marker extraction

4.2.1. Initial marker extraction

The initial markers of specular highlights in the froth images are extracted from the preprocessed data using three methods: Intuitionistic Fuzzy C-Means (IFCM), adaptive thresholding, and morphological reconstruction with opening-and-closing operators. A comparison of the performance of these initial marker extraction methods is illustrated in Fig. 3.

As illustrated in Fig. 3, the IFCM algorithm achieves the best highlight extraction performance, despite suffering from over-extraction in small highlighted regions. ATM performs effectively for small highlight areas but faces issues of incomplete extraction in large highlight regions. While MROC exhibits poor overall extraction performance, it yields satisfactory results in certain localized areas.

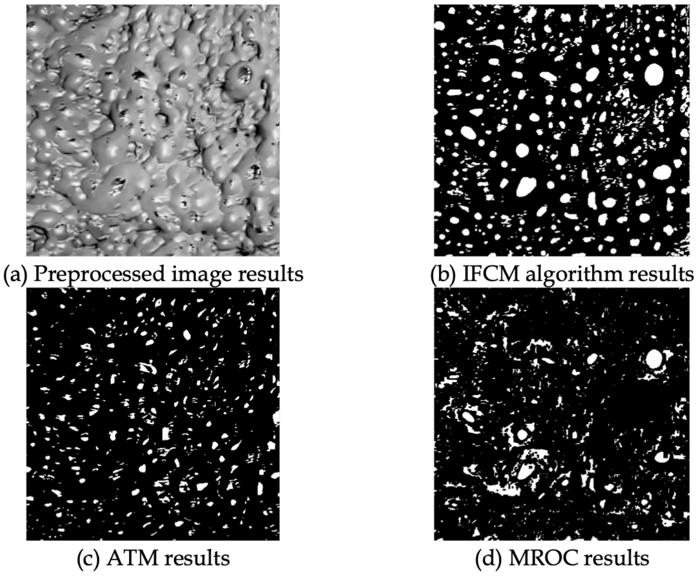

Fig. 3. Performance comparison of initial marker extraction methods

4.2.2 Optimal marker extraction

4.2.2.1. Marker region classification

Following the initial marker extraction, marker region classification is performed, categorizing the regions into small, medium, and large based on the size of the extracted specular highlights. The IFCM, adaptive thresholding, and morphological reconstruction algorithms are then applied to extract highlights for froths in these three size categories, with the results illustrated in Fig. 4.

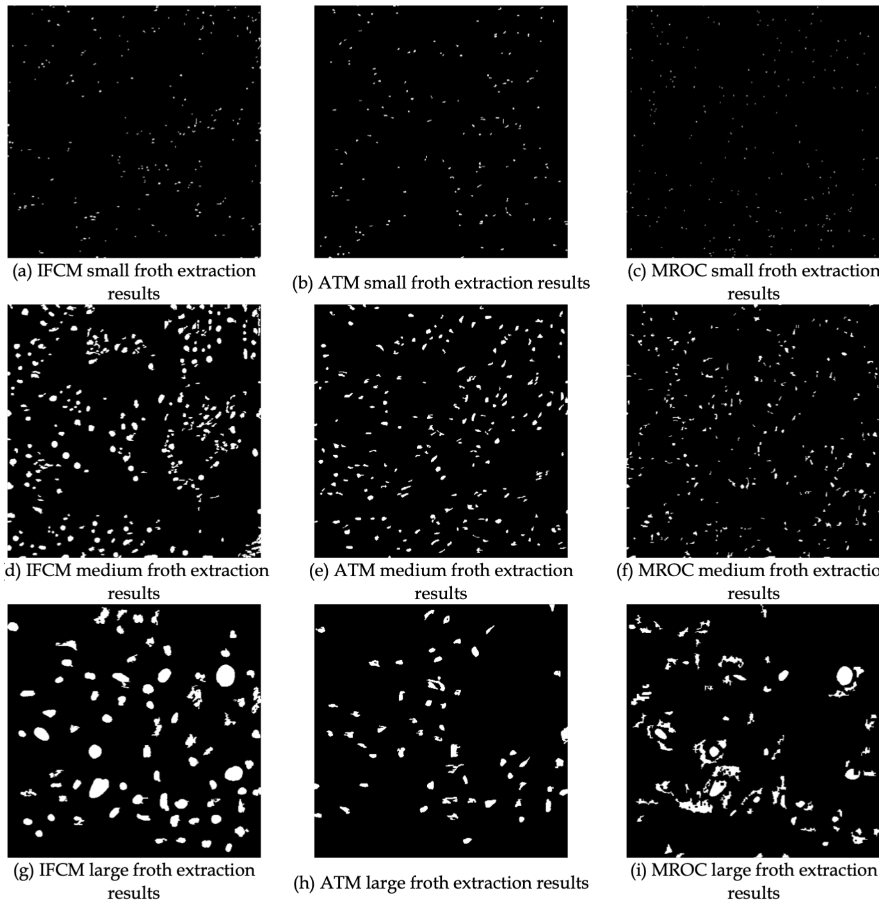

Fig. 4. Extraction results of bubbles with different sizes

As illustrated in Fig.4, variations in the size and quantity of extracted froth highlights across the three algorithms lead to differing performances, though their spatial distributions remain similar. In small froth regions, noise predominates, although some tiny highlights are still detected. Medium froth regions yield the best overall results; the three algorithms exhibit similar highlight distributions while demonstrating complementarity in certain localized areas. Performance varies notably in large froth regions: IFCM achieves a uniform distribution of highlights, whereas ATM detects a lower count and misclassifies some large highlights into medium regions. In contrast, the highlights extracted by MROC exhibit significant adhesion.

4.2.2.2. Marker region merging

Upon completion of froth highlight extraction, overlap correction is performed on the three categories of marker regions individually, followed by marker region merging to extract the optimal foreground markers. The results of the merged markers are illustrated in Fig. 5.

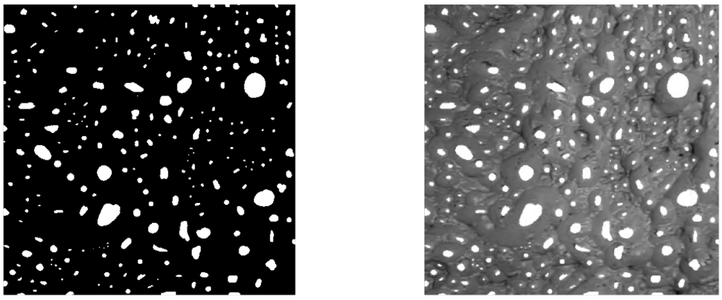

(a)Specular highlight overlap map (b)Merged marker map

Fig. 5. Performance of specular highlight overlap correction and marker fusion

4.3. Froth edge constraint extraction

This paper proposes a froth edge extraction method that combines the Laplacian of Gaussian (LoG) operator with±45°gradient filtering operators. Effective edges are identified via thresholding, where the effective edges are defined as the maximum gradients within the gradient map. Prior to employing the LoG operator for edge extraction, its superiority is validated by comparing its performance against various other edge operators. The edge extraction results of these multiple operators are compared in Fig. 6.

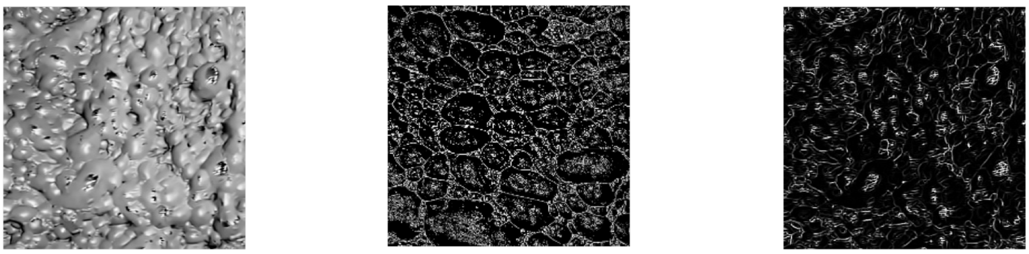

(a)Preprocessed image results (b)Gaussian Laplace results (c)Sobel

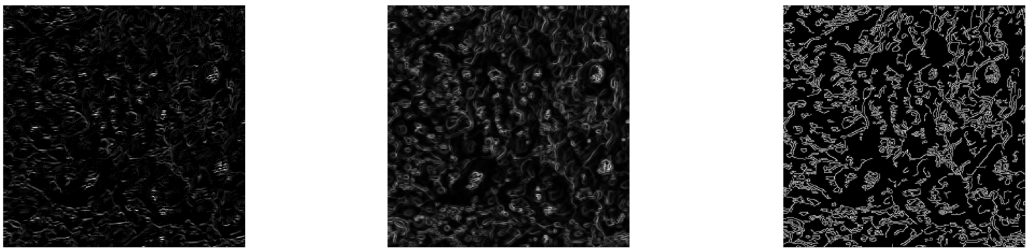

(d) Roberts (e) Prewitt (f)Canny

Fig. 6. Comparison of edge-extraction results

As indicated by the comparative results, the Sobel, Roberts, and Prewitt operators yield discontinuous froth edges and generate excessive internal lines within the froth. The Canny operator extracts redundant texture information that is indistinguishable from the actual edge information. In contrast, the Laplacian of Gaussian (LoG) operator highlights areas with rapid intensity variations while remaining insensitive to smooth transitions, achieving the best edge extraction performance. However, the LoG operator exhibits weak detection sensitivity in the ±45°diagonal directions.

To address this limitation, ±45°gradient filtering operators are introduced to extract diagonal gradients. These results are merged with the edge image obtained from the LoG operator. Subsequently, morphological operations are applied: low-gradient regions are removed, erosion is used to eliminate noise points, and dilation is performed to enhance edge continuity. This process ultimately achieves a comprehensive and complete extraction of froth edges, as illustrated in the workflow in Fig. 7.

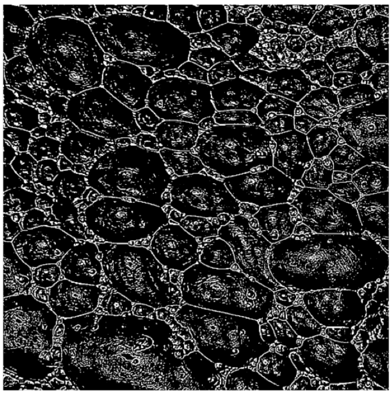

(a)Gaussian Laplacian operator result

(b)positive 45-degree gradient filtering operators result

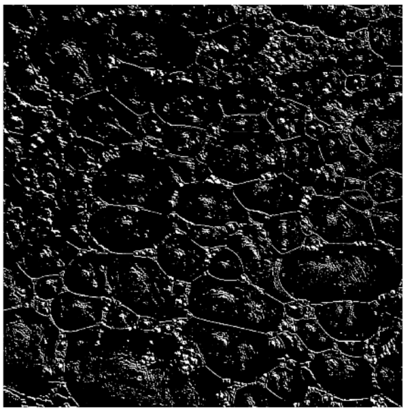

(c)reverse 45-degree gradient filtering operators result

(d)Combined morphological result

Fig. 7. Effectiveness of the Improved edge-extraction method

As shown in Fig. 7(d), the improved method enables the complete extraction of froth edges; however, prominent redundant edges persist within the froth interior. To resolve this, morphological dilation is applied to the extracted foreground markers. The dilation size is carefully selected to be larger than the highlight boundaries but smaller than the froth edges, while ensuring that no adhesion occurs between the markers after dilation. By subtracting these processed markers from the edge extraction results shown in Fig. 7(d), clear and continuous froth edges are obtained, effectively eliminating internal interferences. The final results of the edge constraint extraction are illustrated in Fig. 8.

Compared to the constraint lines in Fig. 7(d), the refined boundary lines in Fig. 8(a) exhibit higher confidence by effectively eliminating the interference generated by specular highlight regions.

Consequently, an improved watershed algorithm is successfully implemented by employing the specular highlight overlap correction method to generate foreground markers and the multi-edge constraint approach to produce the final merged edge constraints.

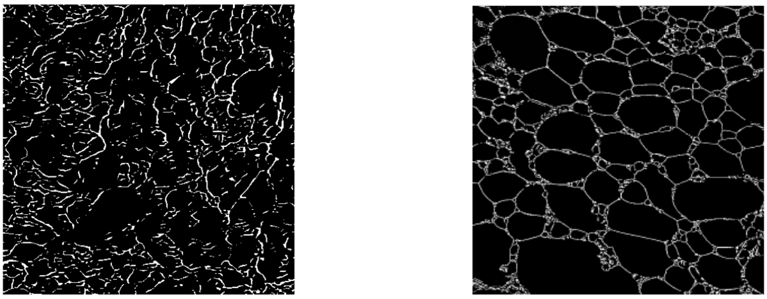

(a)Final constraint line result (b)Multi-edge Constraints result

Fig. 8 Results by removing internal highlighted edges

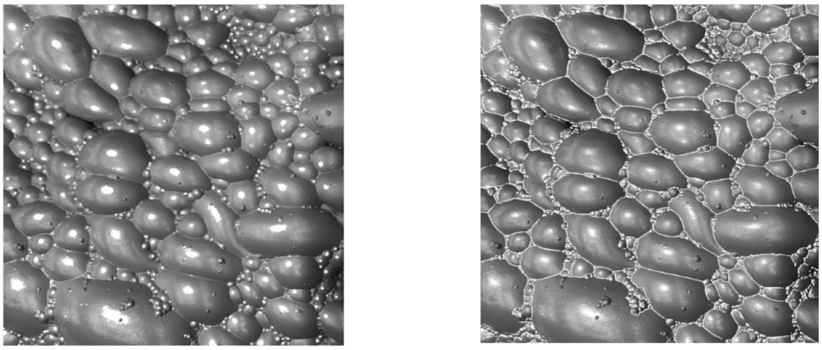

(a)Merged marker map (b)Merged constraint map

Fig. 9. Results of merged markers and merged constraints

4.4. Comparative experiments

Experiments were conducted on three standard froth images to evaluate three segmentation approaches: the methods from (Zhang et al., 2019; Peng et al., 2021), and the proposed algorithm. Zhang et al. (2019) improves the watershed algorithm using optimal markers and edge constraints; this strategy shares a similar underlying logic with the proposed method and has demonstrated superior performance among mainstream watershed-based techniques. Peng et al. (2021) enhances watershed segmentation using a data augmentation network based on conditional Generative Adversarial Networks (cGAN) and a U-Net++ edge segmentation architecture, representing a prominent research direction in deep learning-based image segmentation.

As illustrated in Fig. 10, the proposed algorithm effectively identifies and segments the black boundary lines within the froth images. To enhance segmentation accuracy, black shadows adjacent to the boundaries are identified as background and incorporated into the boundary lines, which accounts for the varying thickness observed in certain sections. Zhang et al. (2019) performs well on prominent boundaries but fails to partition most regions, misidentifying them as a single area. Peng et al. (2021) excludes boundary-adjacent shadows from the background, resulting in inaccurate segmentation lines and overfitting at wider boundaries.

To quantitatively evaluate the results, an image segmentation assessment method based on the Adjusted Rand Index (ARI) is utilized. ARI values range from 0 to 1, with values approaching 1 indicating a higher similarity between the segmentation result and the ground truth. Given the label assignment of the ground truth S and the label assignment of the comparison method S', ARI is expressed as:

$$ARI(S,S') = \frac{\sum_{u,v}\binom{n_{nv}}{2} - [\sum_u n_{u\cdot} \sum_v n_{\cdot v}]/\binom{N}{2}}{\frac{1}{2}[\sum_u \binom{n_{u\cdot}}{2} + \sum_v \binom{n_{\cdot v}}{2}] - [\sum_u n_{u\cdot} \sum_v n_{\cdot v}]/\binom{N}{2}} \tag{35}$$

where n_{nv} denotes the number of pixels having label u in S and the number of pixels having label v in S'; $n_{u\cdot}$ denotes the number of pixels having label u in S and the number of pixels having label v in S'; and v denotes the number of pixels having label v in S'.The symbols with small dots represent a simplified notation in statistics, which is used to denote the summation over specific dimensions. For example,$n_{u\cdot}$represents the summation over the v dimension, that is, fixing u and adding up all the n_{nv} corresponding to v.The symbols with small dots represent a simplified notation in statistics, which is used to denote the summation over specific dimensions.

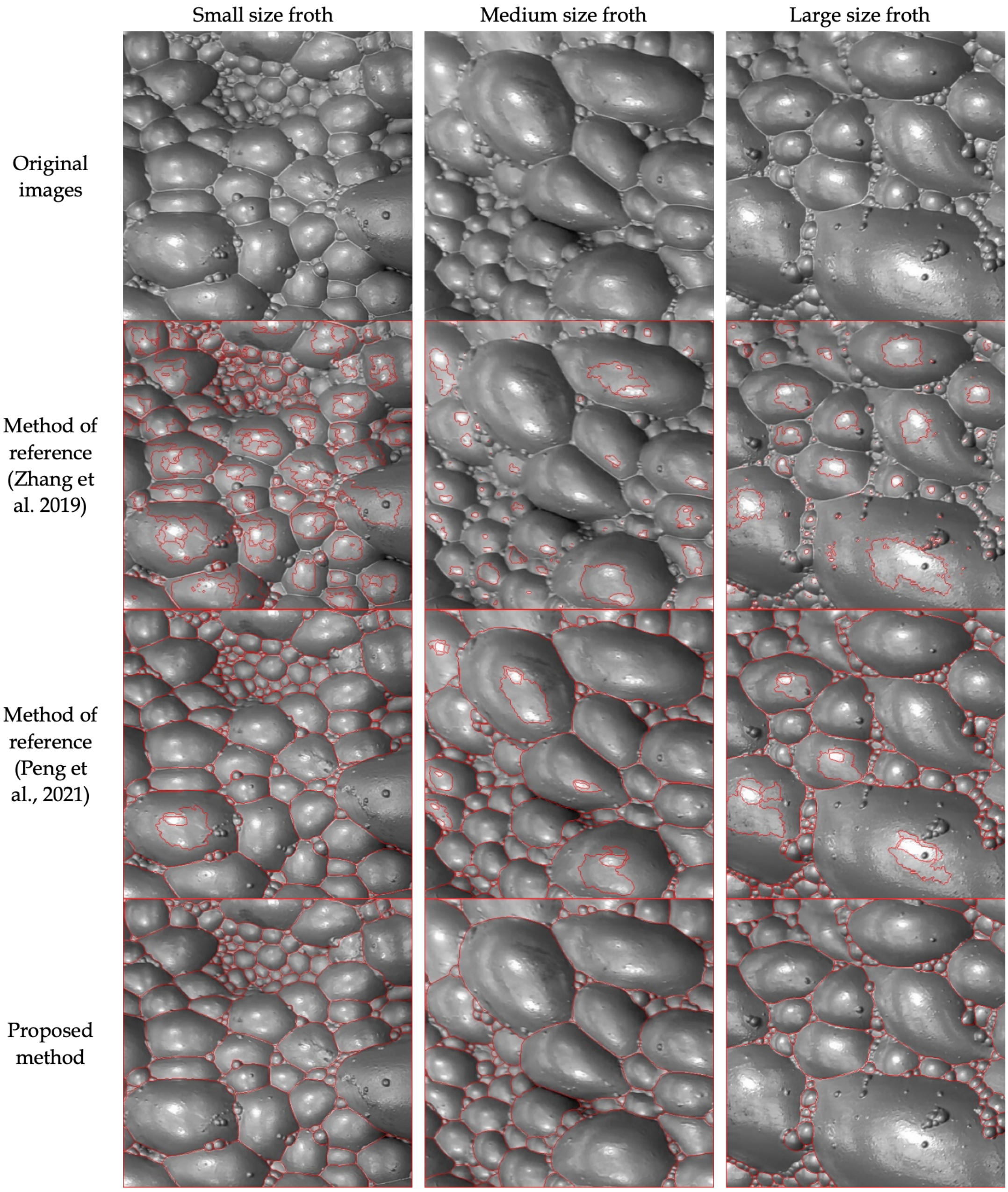

Fig. 10. Comparison of segmentation results by different methods

In this study, 50 froth images were collected from the database and manually annotated by experienced workers to establish the ground truth. The segmentation performance of the proposed improved algorithm was compared against the methods in (Zhang et al., 2019; Peng et al., 2021) based on these manual annotations. The resulting Adjusted Rand Index (ARI) values, calculated relative to the ground truth, are presented in Fig. 11.

The experimental ARI results are illustrated in Fig.11, from which several conclusions can be drawn:

(1) The proposed method yields higher ARI values than the other two approaches, indicating that the improved watershed algorithm achieves a segmentation effect closer to the ground truth.

(2) Compared with the competing methods, the proposed algorithm exhibits smaller ARI fluctuations, reflecting higher stability.

(3) In certain froth images characterized by minimal impurities and uniform bubble sizes, the ARI results of the proposed method and (Peng et al., 2021) are highly comparable.
(4) Zhang et al. (2019) yields inferior segmentation results as it only considers optimal markers and lacks in-depth extraction of constraint lines; as a result, the ARI values of both the proposed method and Peng et al. (2021) significantly outperform those of Zhang et al. (2019).

To further substantiate the comparison, the mean $\overline{R}$ and variance $\overline{\sigma}$ of the ARI results were calculated, along with the sum of the difference ratios $S_{\overline{R}}$ and $S_{\overline{\sigma}}$ between the proposed method and the other two algorithms. These metrics provide a more direct demonstration of why the improved watershed algorithm achieves superior segmentation performance compared to the two competing algorithms.

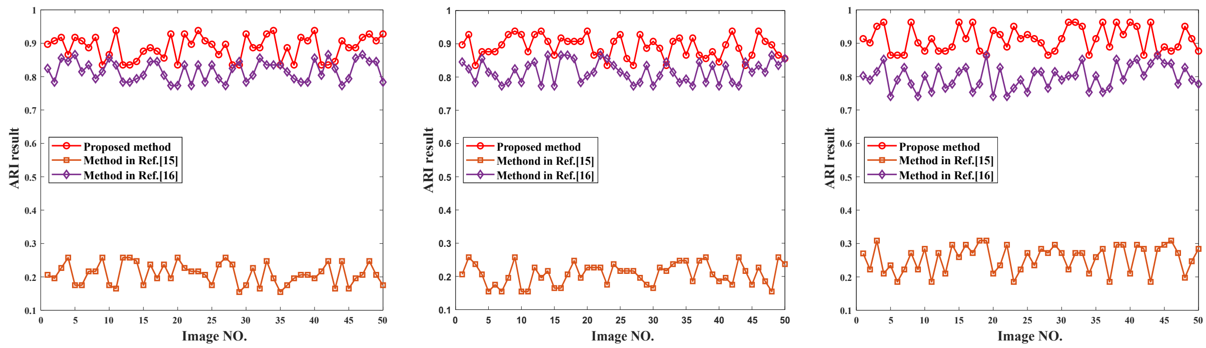

(a) ARI of three methods for small froths (b) ARI of three methods for medium froths (c) ARI of three methods for large froths

Fig. 11. Comparison of ARI of the three methods for each size of froth

Table 1. The statistical ARI results of the three methods

Statistic	Method in (Zhang et al., 2019)			Method in (Peng et al., 2021)			Proposed method		
	Small froth	Medium froth	Large froth	Small froth	Medium froth	Large froth	Small froth	Medium froth	Large froth
$\overline{R}$	0.2881	0.2016	0.2469	0.7617	0.8241	0.8012	0.8185	0.8763	0.9163
$S_{\overline{R}}$	0.5304	0.6747	0.6694	0.0568	0.0522	0.1151	-	-	-
$\overline{\sigma}$	0.1434×10^{-2}	0.1106×10^{-2}	0.1434×10^{-2}	0.1106×10^{-2}	0.0801×10^{-2}	0.1757×10^{-2}	0.0705×10^{-2}	0.0740×10^{-2}	0.1014×10^{-2}
$S_{\overline{\sigma}}$	-0.0729×10^{-2}	-0.0366×10^{-2}	-0.0420×10^{-2}	-0.0401×10^{-2}	-0.0061×10^{-2}	-0.0743×10^{-2}	-	-	-

As demonstrated in Table 1, the proposed method achieves the highest mean ARI values across small, medium, and large froth categories, delivering superior segmentation performance compared to the other two methods. Furthermore, the variance of the proposed method is lower than those reported in (Zhang et al., 2019; Peng et al., 2021), indicating that the algorithm consistently yields reliable segmentation results for froth images characterized by bright edges or dark patches. These findings validate the effectiveness and robustness of the improved algorithm.

5. Conclusions

The watershed algorithm based on markers and edge constraints is a mainstream approach for froth segmentation. In this framework, extracting accurate markers and complete constraint lines is essential. However, markers are frequently misled by specular highlights, and constraint lines often remain incomplete due to image blurring. Consequently, this paper proposes an improved watershed algorithm based on specular highlight overlap correction and multi-edge constraints. The main contributions are three-fold:
(1) Foreground marker extraction using multi-algorithm combinations: To address the complexity of froth images, the IFCM algorithm, adaptive thresholding, and morphological reconstruction are employed to extract and classify foreground markers into large, medium, and small categories.

Overlap correction is applied across these sizes to eliminate noise while retaining authentic markers, thereby enhancing the completeness and accuracy of the foreground markers.

(2) Refinement of segmentation lines using multi-edge constraints: To resolve the issue of fragmented constraint lines, the Laplacian of Gaussian (LoG) operator is used to extract horizontal and vertical constraints, supplemented by ±45°gradient operators for refinement. This approach mitigates incomplete extraction caused by non-uniform brightness and low contrast. Experimental results demonstrate that the extracted lines are closer to the ground truth, with an average ARI of 91.63% and a variance of 0.1014*10-2 for small froth.

(3) Size-dependent marker region merging: By leveraging the varying confidence levels of the three algorithms across different sizes, specific merging strategies are designed: noise removal for small froth, dynamic area-based extraction for medium froth, and correction-merging for large froth. This ensures effective highlight extraction across all froth size categories.

References

MORAR, S.H., HARRIS, M.C., BRADSHAW, D.J. *The use of machine vision to predict flotation performance.* Minerals Engineering, 2012, 36–38, 31–36.

ALDRICH, C., MARAIS, C., SHEAN, B.J., CILLIERS, J.J. *Online monitoring and control of froth flotation systems with machine vision. A review.* International Journal of Mineral Processing, 2011, 96(1), 1–13.

BHONDAYI, C. *Flotation froth phase bubble size measurement.* Mineral Processing and Extractive Metallurgy Review, 2022, 43(2), 251–273.

GUO, Q., WANG, Y., YANG, S., XIANG, Z. *A method of blasted rock image segmentation based on improved watershed algorithm.* Scientific Reports, 2022, 12, 1–21.

LIANG, X.M., TIAN, T., LIU, W.T., NIU, F.S. *Flotation froth image segmentation based on highlight correction and parameter adaptation.* Mining, Metallurgy & Exploration, 2020, 37(2), 467–474.

ZHANG, W., JIANG, D. *The marker-based watershed segmentation algorithm of ore image.* In: IEEE International Conference on Communication Software and Networks (ICCSN 2011), 2011.

JAHEDSARAVANI, A., MARHABAN, M.H., et al. *Development of a new algorithm for segmentation of flotation froth images.* Minerals Engineering, 2014, 66, 102–109.

LANG, F.L., JIANG, D.L. *Floatation froth image segmentation algorithm based on mathematical morphology and wavelet.* In: The Second International Conference on Theoretical and Mathematical Foundations of Computer Science (ICTMF 2011), 6 May 2011.

MOGA, A.N., GABBOUJ, M. *Parallel marker-based image segmentation with watershed transformation.* Journal of Parallel and Distributed Computing, 1998, 51(1), 27–45.

SALMAN, N. *Image segmentation based on watershed and edge detection techniques.* International Arab Journal of Information Technology, 2006, 3(2), 104–110.

DING, W., ZHANG, Z., GUO, X., SU, L., HUA, C. *EWSeg: A fast segmentation algorithm for images based on edge linking and watershed constraints.* Measurement Science and Technology, 2024, 35(4), 045407.

ZHANG, Y., GUI, W.H., YANG, C.H. *Measurement of flotation froth color and size based on computer vision.* Journal of Central South University (Science and Technology), 2008, 39(1), 140–145.

RAPAKA, S., KUMAR, P.R., KATTA, M., LAKSHMINARAYANA, K., KUMAR, N.B. *A new segmentation method for non-ideal iris images using morphological reconstruction FCM based on improved DSA.* SN Applied Sciences, 2021, 3, 1–15.

XIE, D.H., LU, M., XIE, Y.F., LIU, D., LI, X. *A fast threshold segmentation method for froth image based on the pixel distribution characteristic.* PLOS ONE, 2019, 14(1), e0210233.

ZHANG, H., TANG, Z., XIE, Y., GAO, X., CHEN, Q. *A watershed segmentation algorithm based on an optimal marker for bubble size measurement.* Measurement, 2019, 138, 182–193.

PENG, C., LIU, Y., GUI, W., TANG, Z., CHEN, Q. *Bubble image segmentation based on a novel watershed algorithm with an optimized mark and edge constraint.* IEEE Transactions on Instrumentation and Measurement, 2021, 71, 1–10.

ZHANG, W., LIU, D., WANG, C., LIU, R., WANG, D., YU, L., WEN, S. *An improved Python-based image processing algorithm for flotation foam analysis.* Minerals, 2022, 12(9), 1126.

TANG, C., GUO, J., ZHANG, H., XIE, Y., ZHONG, Y. *Zinc flotation foam image segmentation algorithm based on improved I-Attention U-Net.* Journal of Hunan University (Natural Sciences), 2023, 50(2), 12–22.

XUE, Y., LIU, Z., LI, Z., ZHU, P. *CT image segmentation method of composite material based on improved watershed algorithm and U-Net neural network model*. Journal of Shanghai Jiaotong University (Science), 2023, 28(6), 783–792.

CHEN, J., ZHU, S., LUO, W. *Instance segmentation of underwater images by using deep learning.* Electronics, 2024, 13(2), 274.